Article

Permafrost Early Deformation Signals before the Norilsk Oil Tank Collapse in Russia

Peng Zhang [1], Yan Chen [1], Youhua Ran [2] and Yunping Chen [1,*]

1   School of Automation Engineering, University of Electronic Science and Technology of China, No. 2006, Xiyuan Avenue, West Hi-Tech Zone, Chengdu 611731, China
2   Heihe Remote Sensing Experimental Research Station, Key Laboratory of Remote Sensing of Gansu Province, Northwest Institute of Eco-Environment and Resources (NIEER), Chinese Academy of Sciences (CAS), 320 Donggang West Road, Lanzhou 730000, China
*   Correspondence: chenyp@uestc.edu.cn

Abstract: Despite the profound roles of surface deformation monitoring techniques in observing permafrost surface stability, predetermining the approximate location and time of possibly occurring severe permafrost degradation before applying these techniques is extremely necessary, but has received little attention. Taking the oil tank collapse accident in the Norilsk region as a case, we explored this concern by analyzing the permafrost deformation mechanisms and determining early surface deformation signals. Regarding this case, we firstly applied the Small Baseline Subset Interferometric Synthetic Aperture Radar (SBAS-InSAR) technique to obtain its permafrost surface deformation rate, then utilized a sine model to decompose its interannual deformation and seasonal deformation, and finally compared the relationship between the topographic slope and deformation rate. Based on experimental results, we reveal that when the annual average temperature continuously increases at a rate of 2 °C/year for 2∼3 consecutive years, permafrost areas with relatively large topographic slopes (>15°) are more prone to severe surface deformation during the summer thaw period. Therefore, this paper suggests that permafrost areas with large topographic slopes (>15°) should be taken as the key surveillance areas, and that the appropriate monitoring time for employing surface deformation monitoring techniques should be the summer thawing period after a continuous increase in annual average temperature at a rate of 2 °C/year for 2∼3 years.

Keywords: permafrost degradation; deformation; SBAS-InSAR; early warning

1. Introduction

The water in the active layer of the permafrost continuously changes between the solid and liquid states with the alternation of seasons. Since the ice approximately takes 9% more volume than water, the seasonal ice–water phase change process will lead to changes in the volume of permafrost. This process in turn will cause periodic freeze-swelling and thaw-sinking of the ground surface and seriously damage the stability of engineering infrastructure in the region [1–3]. Another study shows that the global average near-surface temperature has climbed at a rate of approximately 0.6 °C/10-years in the past 30 years. Moreover, the rate of increase in near-surface temperature in permafrost areas is two to three times the rate of the increase in global temperature. Even for CO_2, the release of which from the melting of permafrost has further intensified global warming [4–8]. In this context, a series of permafrost degradation problems, such as the melting of subsurface ice in permafrost and the increase in active layer thickness, are becoming increasingly significant. The resulting surface deformation may undermine the stability of buildings and infrastructure on permafrost and lead to surface deformation disasters [9–14]. For instance, freeze–thaw hazards from global climate warming and China–Russia permafrost degradation induce uneven deformation of the China–Russia crude oil pipeline (CRCOP), which threatens the CRCOP's operational safety [15]; seasonal permafrost surface displacement

in the Litang River alluvial area imperils the construction and normal operation of the Sichuan Tibet Railway [16]; landslides of the Bei'an to Heihe Expressway in China are often caused by uneven degradation and settlement from the warming climate, which disrupts highway operational safety [17].

Facing the situation that permafrost surface deformation disasters seriously endanger the infrastructure, there has been a continuous focus on disaster mechanisms in previous studies. Qi et al. [18] found that the disasters mainly result from several simultaneous processes: thaw settlement from the permafrost degradation, creep, and freeze–thaw cycle. Among them, the first process has been considered to be the most problematic and important. Chang et al. [19] explained that "the thermal gathering effect" and non-uniform spatially distributed underground ice also induced surface deformation differences. Moreover, Luo et al. [20] also emphasized that topographic slope factors would influence permafrost deformation. However, even though the mechanisms and influencing factors of permafrost deformation have been extensively studied, these results are still applied insufficiently to the existing deformation monitoring techniques. These inadequate applications make the current monitoring of permafrost surface deformation hazards still mainly after-the-fact monitoring and difficult to prevent in advance.

Current surface deformation monitoring techniques mainly include traditional monitoring technology and MT-InSAR (Multi-temporal InSAR) technology, which are widely applied to the task of monitoring permafrost stability. The traditional deformation monitoring methods, such as leveling, Global Positioning System Interferometric Reflectometry (GPS-IR) observations, and settlement gauges, are more accurate in small-range monitoring. These techniques, however, generally cannot meet the needs of large-scale and long-term deformation monitoring [21–23]. D-InSAR (Differential InSAR) and MT-InSAR technologies, as new technical tools, provide the possibility of large-scale and long-term permafrost monitoring, which have been widely used and have achieved good results [24–27]. Both traditional monitoring methods and MT-InSAR technology require predetermined monitoring areas and monitoring time can narrow the observation areas, reduce technical costs, and improve monitoring accuracy to facilitate the equipment deployment for on-site monitoring or download relevant data for model inversion [28,29]. However, there are still relatively few answers on how to predetermine where and when severe surface deformation is likely to occur in permafrost areas.

Taking the collapse of oil tanks in the permafrost area of Norilsk, Russia on 29 May 2020, as a case, this paper gives answers by exploring permafrost deformation mechanisms and analyzing early deformation signals before the Norilsk oil tank collapse accident. Concerning this case, we first apply the SBAS-InSAR technique to obtain its deformation rate, then utilize a sine decomposition model to calculate interannual deformation and seasonal deformation, and finally compare topographic slope and surface deformation rate distribution. As per experimental results, we reveal the causes and mechanisms of permafrost deformation, explore the early deformation signals before the accident, and specify how to determine the regions and time periods where severe deformation may occur.

2. Study Area and Materials

On 29 May 2020, the Heat and Power Plant No. 3 (HPP-3) located in the Norilsk region, a city in Siberia, Russia, experienced an oil tank collapse accident [30,31]. In accordance with statistics, it released 21,000 cubic meters (17,500 tons) of diesel fuel into the local Dardikan and Ambanaya rivers and contaminated areas up to 350 square kilometers, severely polluting the river environment in the surrounding area [32,33]. The BBC Russia News claimed that the accident was the second largest oil spill in Russian history [34]. The clean-up of the oil spill is expected to take five to ten years to complete and will cost up to $1.5 billion. In order to explore the antecedents of this accident and to investigate the factors leading to permafrost surface deformation hazards, a 10 km buffer zone (total around 314 km^2) centered on the accident site (69°19′37.74″N, 87°56′1.86″E) is chosen as the study area in this paper. Figure 1a,b show the location and land surface types of the

study area. According to Shur et al. [35], the permafrost types of climate-driven, climate-driven/ecosystem-modified, climate-driven/ecosystem-protected, ecosystem-driven, and ecosystem-protected are the most vulnerable, thermally stable and thaw unstable, degraded, degrading, and most sensitive to climate warming, respectively. Figure 1c indicates that the study area belongs to "Climate-driven/ecosystem-modified" permafrost. It implies that the melting stability of the study area is poor and the surface deformation disaster from permafrost degradation is easy to occur [36–38].
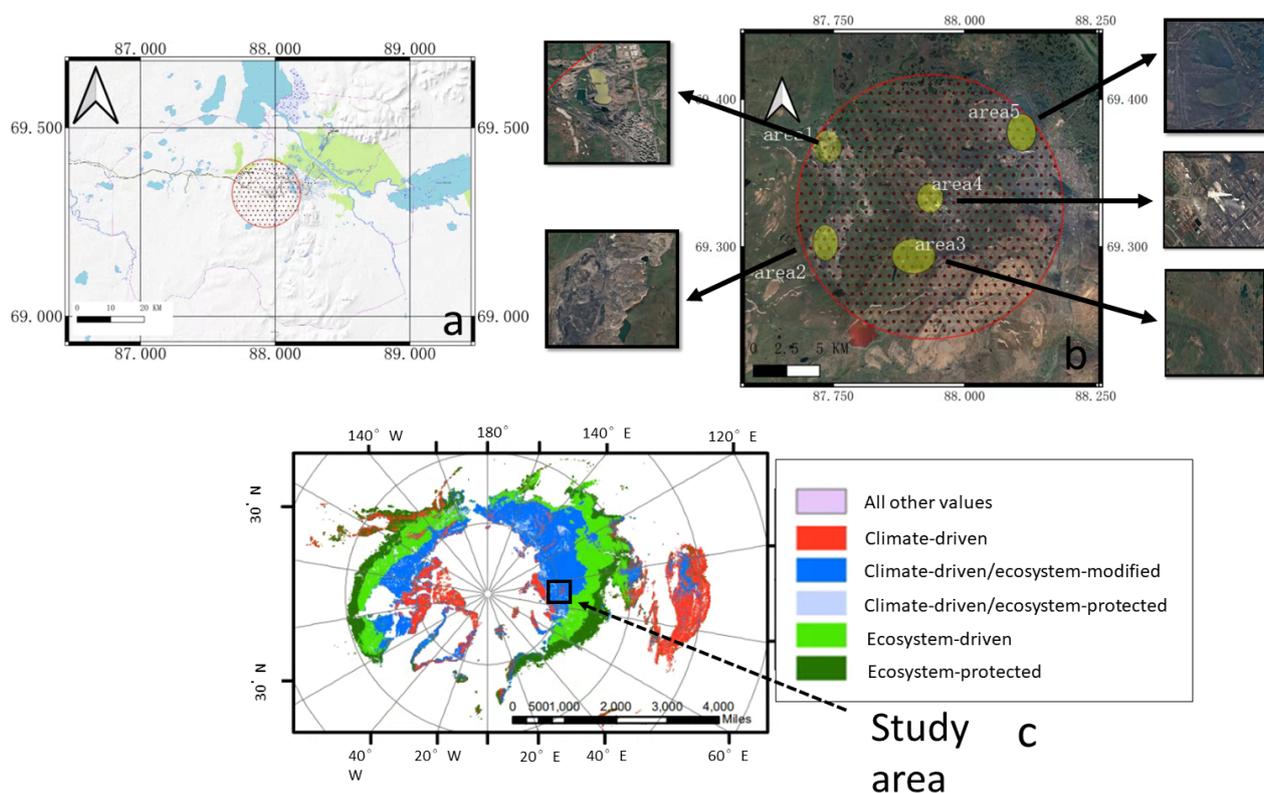
Figure 1. Distribution of surface types in the 10 km buffer zone around the collapse site in the Norilsk region: (**a**) shows the geographical location of the study area; (**b**) represents a satellite map of the study area, where area1–area5 represent five typical features: buildings, hills, the plant where the tank collapse occurred, vegetation, and water, respectively; and (**c**) shows biophysical permafrost distribution results.

In this paper, we first use the single look complex (SLC) data of the 66 Sentinel-1B images (https://scihub.copernicus.eu/ (accessed on 24 March 2022)), supplemented by the AUX_POEORB precision orbit data (https://scihub.copernicus.eu/gnss/#/home (accessed on 24 March 2022)) and the 30 m spatial resolution ASTER-GDEM surface elevation data to analyze the surface deformation in the study area. The Sentinel 1b data were imaged over time from 25 August 2018, to 24 December 2020, with an orbital mode of VV+VH, path 136, and frame 363.

Second, this paper employs the soil water content data at each depth (0–7 cm, 7–28 cm, 28–100 cm, 100–289 cm) from the ERA5-Land monthly average dataset and soil parameter dataset (as shown in Table 1) [39,40] was used to obtain the freeze–thaw seasonal thermal conductivity of the study area.

Third, the 8-day synthetic surface temperature data from MODIS (MYD11A2) are selected to serve as the large-scale land surface temperature data in the study area to calculate the interannual melting depth. Additionally, topographic slope data using the ALOS 30 m spatial resolution DSM are applied to analyze the relationship between slope and deformation.

Table 1. The data layers in the soil parameters dataset used in this paper.

Attributes	Unit
Volumetric fraction of gravels	$\mathrm{cm}^3/\mathrm{cm}^3$
Volumetric fraction of soil organic matters (SOM)	$\mathrm{cm}^3/\mathrm{cm}^3$
Volumetric fraction of sand	$\mathrm{cm}^3/\mathrm{cm}^3$
Thermal conductivity of unfrozen saturated soils	$\mathrm{W}\cdot\mathrm{m}^{-1}\cdot\mathrm{K}^{-1}$
Thermal conductivity of frozen saturated soils	$\mathrm{W}\cdot\mathrm{m}^{-1}\cdot\mathrm{K}^{-1}$
Thermal conductivity of dry soils	$\mathrm{W}\cdot\mathrm{m}^{-1}\cdot\mathrm{K}^{-1}$

Note: The data selected in this paper are all simulated data under the Noah-LSM model. Moreover, the dataset is stored in binary format with a spatial resolution of 30 arc seconds and covers 43,200 columns (longitude) and 21,600 rows (latitude) of global data from 180°W to 180°E and from 90°N to 90°S. The above information is quoted from http://globalchange.bnu.edu.cn/research/soil5d.jsp (accessed on 21 March 2022).

3. Methods

3.1. Long-Term Surface Deformation Monitoring

The widely used MT-InSAR techniques mainly include the permanent scatterer InSAR (PS-InSAR) proposed by Ferretti et al. [41] and the Small Baseline Subset InSAR (SBAS-InSAR) proposed by Beradino et al. [42]. This paper uses the SBAS-InSAR technique to monitor the permafrost surface deformation in the study area over an extended period of time. The main principle is shown in Equation (1). x and r are the pixel azimuth and range direction coordinates, respectively. $\Delta\varphi_i(x,r)$ represents the interferometric phase of image pixel (x,r). t_2 and t_1 are the master and slave image acquisition times, respectively. When the surface displacement of the radar line of sight (LOS) is assumed as 0 at the reference moment t_0, $d(t_2,x,r)$ and $d(t_1,x,r)$ denote the radar cumulative LOS displacements of the master and slave images relative to the moment t_0, respectively. λ is the wavelength of the radar signal. $\Delta\varphi^i_{top}$ is the topographic phase. $\Delta\varphi^i_{APS}$ is the atmospheric delay phase. $\Delta\varphi^i_{noise}$ represents the orbital error, system thermal dryness, etc.

$$
\begin{aligned}
\Delta\varphi_i(x,r) =&\, \varphi_2(x,r) - \varphi_1(x,r) \\
\approx&\, \frac{4\pi}{\lambda}\left(d(t_2,x,r) - d(t_1,x,r)\right) + \Delta\varphi^i_{top} + \Delta\varphi^i_{APS} + \Delta\varphi^i_{noise}
\end{aligned}
\tag{1}
$$

The SBAS-InSAR experimental steps in this paper are based on the SARscape: (1) Pre-processing: After importing the SLC data of 66 Sentinel-1B images and the corresponding AUX_POEORB precision orbit data, the study area is cropped to obtain the multi-temporal SAR images. (2) Baseline estimation and generation of connection diagrams: the maximum spatial and temporal baselines are set as 1% and 120 days, respectively. A total of 275 sets of image pairs meeting the baseline conditions are obtained. The average number of connections per image is 7.24 pairs. (3) Differential interference: This step includes registration, differential interference, flat earth phase removal, interferogram filtering, coherence coefficient calculation, and phase unwrapping. Range looks and azimuth looks are 4 and 1, respectively. The Goldstein method [43] is selected in filtering, with a window size of 64. The unwrapping method is the minimum cost flow [44] (MCF) algorithm, with a coherence threshold is 0.35. (4) Removal of interference pairs: Figure 2 suggests the different results after phase unwrapping (not geocoded). As shown in Figure 2a,b, the interferometric image pairs with at least one whole unwrapping region are preserved. A total of 38 pairs with poor coherence and pairs with even almost all isolated phases are removed, shown in Figure 2c. (5) Orbital refinement: In order to eliminate the residual phase and the still existing phase ramp after unwrapping, 35 ground control points (GCP) shown in Figure 3 are selected. Combining the precision orbit data and 30 m resolution ASTER-GDEM surface elevation data, this paper estimates the orbit refinement and phase offset by using a cubic orbit refinement polynomial. Finally, the slope phase and topographic phase are also removed. (6) Inverse estimation: The first inversion uses the singular value decomposition (SVD) method to calculate the deformation and residual topography of all interferometric image pairs. The second inversion estimation is based on the first estimation, and the effect of

the atmospheric phase is removed by filtering algorithms to obtain the final deformation results on the time series. (7) Geocoding: The surface deformation rates in the radar LOS direction are converted to the vertical direction.
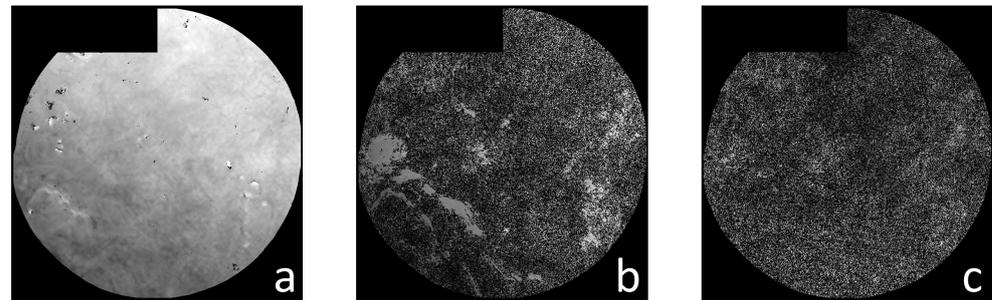
Figure 2. Diagram after the phase unwrapping (not geocoded): (**a**–**c**) demonstrate image pairs with excellent unwrapping effects, retainable unwrapping effects, unwrapping effects to be removed, respectively.
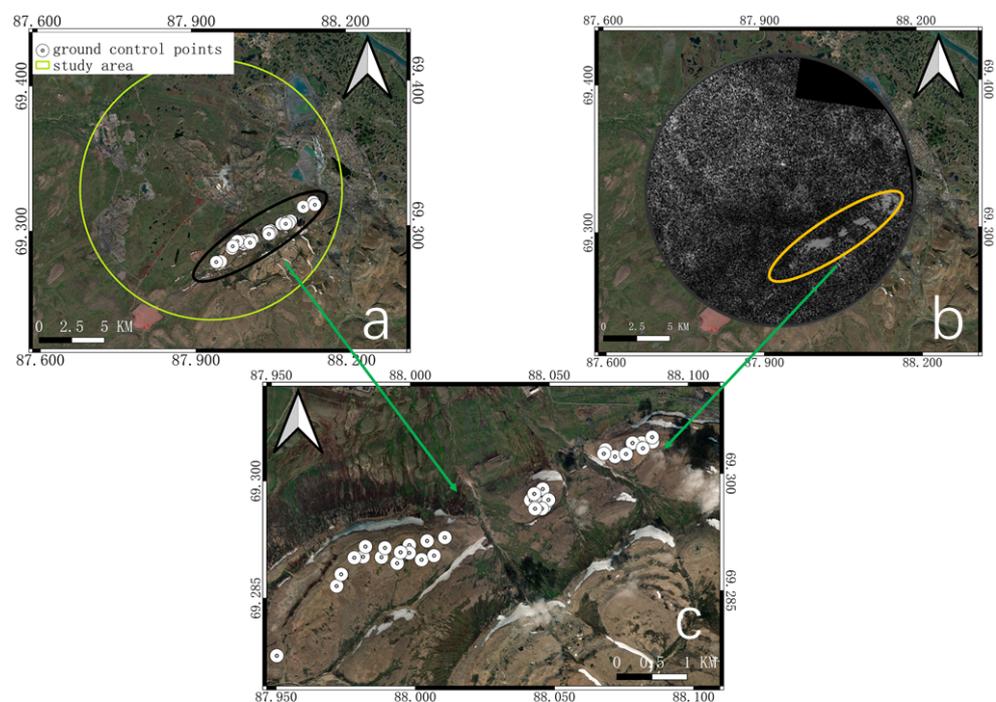
Figure 3. Location of the 35 GCPs: (**a**) shows that the 35 GCPs are mainly distributed in the southeastern study area; (**b**) displays the phase unwrapping results of SAR images, indicating that all 35 GCPs are located in regions with good unwrapping and no significant phase jumps; and (**c**) reveals that the distribution area of GCPs belongs to the flat hilly area, which is suitable for control points.

3.2. Interannual and Seasonal Deformation Decomposition

In this paper, we use a sine model [2,45,46] to decompose the long-term surface deformation variables in the 10×10 pixel range near the tank collapse point into long-term deformation and seasonal deformation.

The model is shown in Equation (2). $D(t)$ represents the long-time deformation variable, v represents the long-time deformation rate, A is the amplitude of the periodic seasonal deformation, T is the period of seasonal fluctuations, ϕ is the initial phase, and c is the residual term.

$$D(t) = v \cdot t + A \cdot \sin(\frac{2\pi}{T} + \phi) + c \qquad (2)$$

In addition, this paper applies the average deformation values of three time periods, early 2020–early 2019, August 2020–August 2018, and late 2019–late 2018 to calculate the

interannual deformation rate. This approach is to prevent the chance of deformation results due to the poor relative interference effect of a certain group.

3.3. Calculation of Thermal Conductivity

Johansen [47] proposed the concept of normalized thermal conductivity K_e based on the research of Kersten [48] and established a semiempirical and semitheoretical model to simulate the thermal conductivity of unsaturated soil. The model is shown in Equation (3), where K_e is the normalized thermal conductivity.

$$\lambda = (\lambda_{sat} - \lambda_{dry})K_e + \lambda_{dry} \tag{3}$$

However, the model was not originally designed specifically for permafrost, and it ignores the significant differences in factors such as soil moisture content and surface temperature in permafrost during the freezing and thawing periods. Therefore, we modified the Johansen model according to the characteristics of permafrost, as shown in Equations (4) and (5), where λ_t and λ_f denote the thermal conductivity of permafrost during the thawing and freezing periods, respectively; λ_{dry} denotes the thermal conductivity of dry soil; $K_{e.t}$ and $K_{e.f}$ denote the normalized thermal conductivity during the thawing and freezing periods, respectively, which can be calculated as per the Balland and Arp model (Equations (6) and (7)) [49]; v_{om} and v_g are the normalized thermal conductivities of the sand, SOM and gravel volume fractions in all soil fractions, respectively; α (0.24 ± 0.04) and β (18.1 ± 1.1) are the volume fractions of sand, SOM and gravel in all soil fractions, respectively; and α (0.24 ± 0.04) and β (18.1 ± 1.1) are the unfreezing experimental data to determine the adjustable parameters.

$$\lambda_t = (\lambda_{sat.t} - \lambda_{dry})K_{e.t} + \lambda_{dry} \tag{4}$$

$$\lambda_f = (\lambda_{sat.f} - \lambda_{dry})K_{e.f} + \lambda_{dry} \tag{5}$$

$$K_{e.t} = S_r^{0.5(1+v_{om}-\alpha v_s - v_g)}\left\{\left[\frac{1}{1+\exp\left(-\beta S_r\right)}\right]^3 - (\frac{1-S_r}{2})^3)^{1-v_{om}}\right\} \tag{6}$$

$$K_{e.f} = S_r^{1+v_{om}} \tag{7}$$

3.4. Calculation of Melting Depth

Based on the one-dimensional heat conduction equation, Stefan [50] proposed a model for predicting the thawing or freezing of sea ice. Although the Stefan problem can only be approximately solved through numerical simulation, many researchers have provided different solutions [51–53]. In this section, we refer to the simple and widely used Stefan equation proposed by Jumikis [54], calculating the interannual thawing depth of permafrost. Equation (8) reveals the formula of the Stefan equation, where d denotes the interannual thawing depth of permafrost (m) and K_t is the freezing thermal conductivity; when using the surface temperature calculation, the values of n_t and n_f are both 1; τ is the length of time (8.64×10^4 s·day^{-1}); L is the latent heat (3.34×10^5 J·kg^{-1}); ρ_b is the soil dry capacity (10^3 kg·m^{-3}); $\Delta\omega$ is the change in water content during the phase change of soil moisture (%). Equation (9) shows that DDT and P are the annual melting index and the annual period, respectively. Since MYD11A2 data have 46 sampling points in a year, here is $P = 46$. For each grid point, the melting index DDT sums up all the sampled values of daily average surface temperature greater than 0 °C during a year.

$$d = \sqrt{\frac{2K_t n_t \tau}{\rho_b L \Delta \omega}} \sqrt{DDT} \tag{8}$$

$$DDT = \int_0^\theta (T_s - T_0)dt \approx \sum_0^\theta \bar{T}(T_s > 0) \tag{9}$$

$$T_0 = 0 \tag{10}$$

During the experimental process, this paper first fills the invalid values of MYD11A2 products by using the spatiotemporal interpolation method. Then, the irradiance brightness is converted into the surface temperature. Finally, the melting depth of the study area is calculated by combining the soil thermal conductivity according to Equation (8). The process is performed on the Google Earth Engine (GEE) platform (https://earthengine. google.com/ (accessed on 25 March 2022)).

4. Results
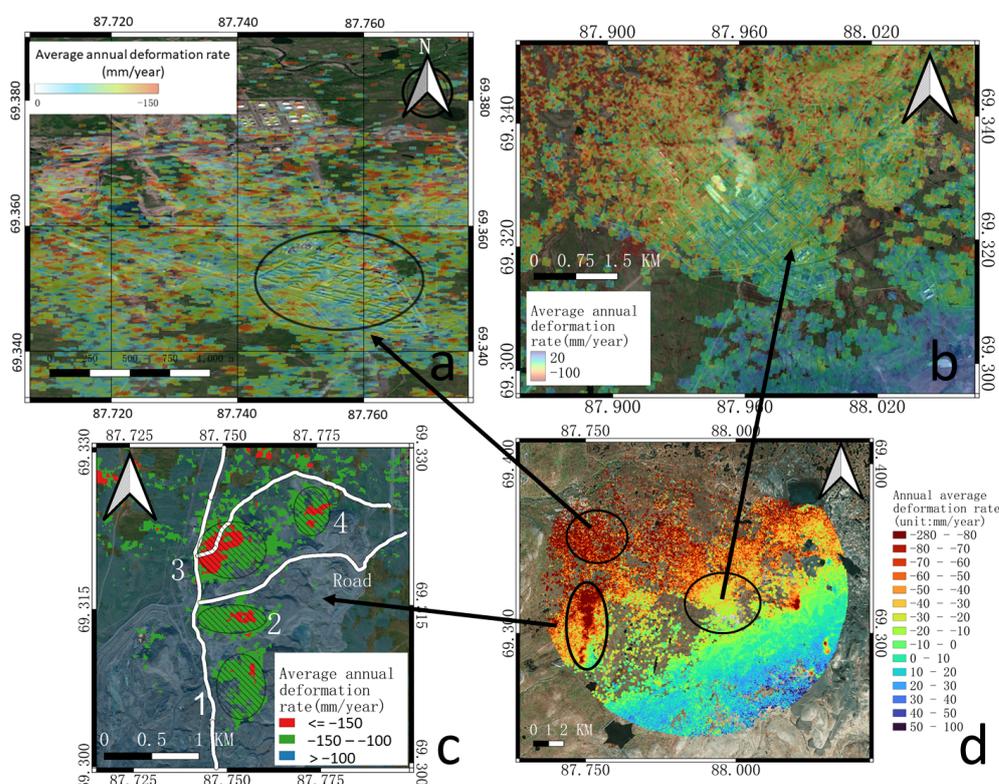
4.1. Surface Deformation Rate Distribution

The surface deformation results in most parts of the study area were already extracted except for the vegetation-covered areas where severe spatial and temporal decoherence effects make it difficult to accurately calculate the surface deformation rates. Figure 4 shows the distribution of the annual average surface deformation rate from August 2018 to December 2020 in the vertical direction. As it can be seen from Figure 4, the deformation in the study area shows a trend of weak uplift–subsidence–severe subsidence from southeast to northwest, which is caused by the deformation rate differentiation of non-homogeneous ground features.
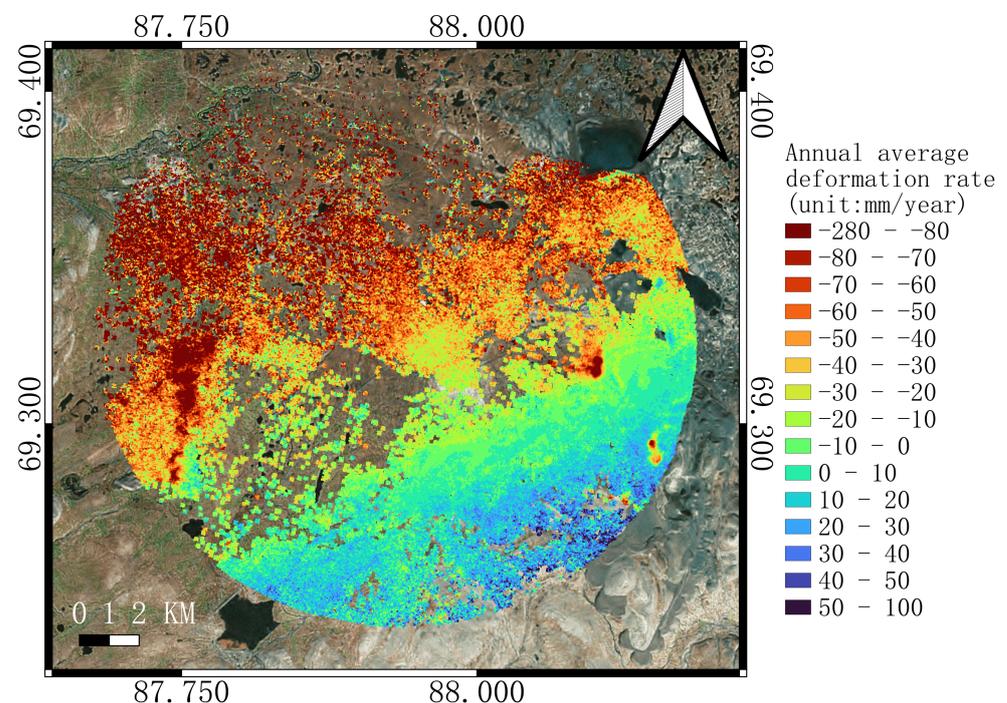
Figure 4. Distribution of annual average surface deformation rates in a 10 km buffer zone around a power plant in the Norilsk region: positive values (blue areas) represent uplift and negative values (green, yellow and red areas) represent subsidence.

The uplifting areas, with the minimal increase, are mainly located in the southeastern hills, where the flat topography and the lack of pressure on the surface from large buildings deny the possibility of severe deformation or landslide hazards. The average deformation rate of the study area is −30.81 mm/year, which indicates that the overall area exhibits

a sinking trend, among which the western, northwestern, and central areas are the most significant. The plant where the oil tank collapse occurred is located in the center of the study area, where the annual average subsidence rate is approximately −30 mm/year (Figure 5b). At the same time, there is also significant subsidence in the northwestern town area, where the subsidence rate can reach −100 to −150 mm/year (Figure 5a). The reason for the high subsidence rates in these two areas is that the large interior buildings or infrastructures increase the effective stress on the ground surface, which gradually compacts the ground and thus reduces the soil porosity, resulting in non-plastic deformation and eventually leading to large subsidence. Moreover, Figure 5c verifies that four landslide hazard potential sites are distributed along the highway in the western steep hill areas, and their surface deformation shapes a subsidence funnel. The average subsidence rates in these funnel centers are greater than −150 mm/year and even reach a maximum of −280 mm/year. This serious deformation may be due to repeated freezing and thawing of the ground surface and the absence of vegetation cover, allowing seasonal snow and ice melt to drive loosening and slippage of the hill soil, coupled with the proximity of the area to the town, human activities also increase the potential risk of landslides.


Figure 5. Deformation rate differentiation of non-homogeneous ground features: (**a**–**c**) take on the deformation rate distribution of the northwestern town area, the central plant area, and the western steep hill area, respectively; (**d**) is from Figure 4.

4.2. Interannual Deformation and Seasonal Deformation Decomposition

Figure 6 shows that the actual total deformation (Figure 6a) of the tank collapse site can be decomposed into interannual surface subsidence (Figure 6b) and periodic seasonal deformation (Figure 6c).

First, Figure 6 reflects that the actual total deformation has the following characteristics. (1) From the perspective of seasonal characteristics, the actual total deformation during the winter freezing period is significantly smaller than that during the summer thawing period. Specifically, the surface rises slightly during the winter freezing period, and the surface sinks relatively faster during the summer thawing period. (2) From the perspective of interannual characteristics, the actual total deformation during August 2018–August

2020 almost always gradually settles over time. The collapse of the fuel tank occurred until 29 May 2020, when the surface actually sank approximately 60–70 mm relative to August 2018.
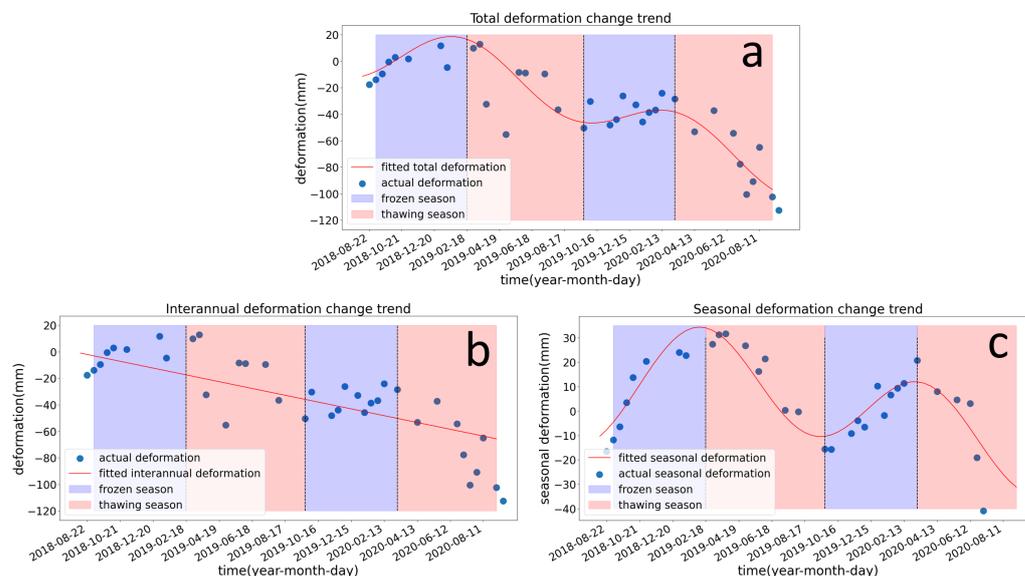

Figure 6. Actual total deformation, interannual deformation, and seasonal deformation calculation results for the area near the tank collapse site from August 2018 to August 2020: (**a**) the trend of actual total surface deformation obtained by the SBAS-InSAR technique; (**b**) the trend of interannual surface deformation; and (**c**) the trend of periodic seasonal surface deformation.

Figure 6b shows that the interannual land surface in the area of the tank collapse site always sinks at a rate of approximately −35 mm/year during 2018–2020. Apart from that, we also find that the seasonal deformation (Figure 6c) has an annual cyclic sinusoidal trend— summer subsidence and winter uplift, with a general sinking depth of approximately 10–20 mm in summer and a maximum uplifting height of approximately 30 mm in winter. This is consistent with the "seasonal deformation characters" in Figure 6a: the surface slightly rises during the freezing period in the winter, while the surface sinks faster during the melting period in the summer. This winter result may be due to a slight surface uplift in winter offsetting the interannual sinking deformation trend. Whereas, the area where occurred the tank collapse undergoes steeply increasing settlement in summer. This serious subsidence is due to the combination of summer thawing and sinking and the interannual sinking trend.

4.3. Effect of Annual Average Air Temperature on Interannual Melting Depth

Figure 7a,b represent the trends in interannual melting depth and air temperature in the study area during 2010–2020, respectively. Figure 7a displays that the annual average air temperature fluctuates during 2010–2020, but increases rapidly at a rate of 2 °C/year during 2018–2019. The interannual melting depth of permafrost in the study area also fluctuates, but gradually deepens during 2017–2020 (Figure 7b), which is consistent with the trend in Figure 6b. This result indicates that the increasing annual average air temperature in 2018–2020 melted more permafrost subsurface ice, deepened the interannual melting depth, and moved down the permafrost table year by year. The consequence is that surface subsidence around the tank gradually accumulates, and the permafrost surface stability is gradually destroyed, eventually causing uneven surface settlement.
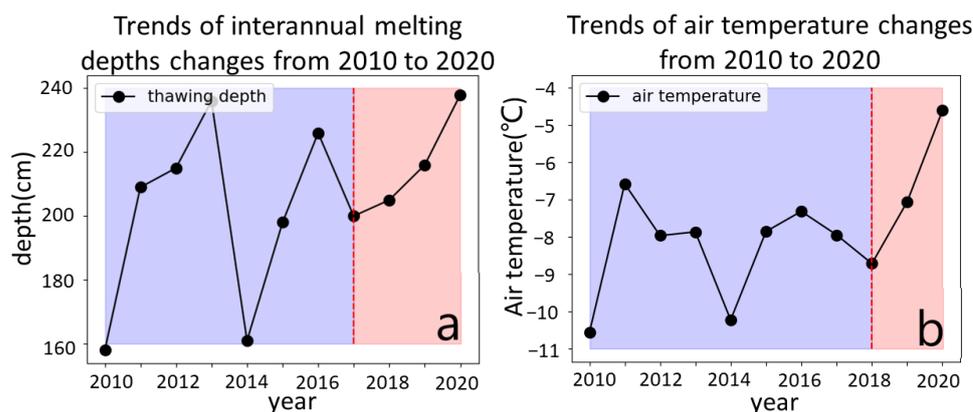
Figure 7. Trends of interannual melting depth and annual average air temperature over the period 2010–2020: (**a**) interannual melting depth; and (**b**) annual average air temperature.

### 4.4. Subsurface Ice Melting Process during the Summer Thawing Period

On account of the fact that changes in soil water content are related to the melting or freezing of subsurface ice, we chose the soil water content data at different depths from the ERA5-land dataset to embody the process of subsurface ice changes. Figure 8b shows the subsurface ice melting trend at each depth of permafrost (0–7 cm, 7–28 cm, 28–100 cm, 100–289 cm) during the summer thaw period in 2020. (1) April–May: subsurface ice began to melt at each soil depth, and the melting rate of the first three layers was faster than that of the fourth layer. This melting rate is probably because the ice in the soil gradually melts as the temperature rises (Figure 8a) and as the infiltration of melting snow erodes. In addition, the reason the shallow soil melts faster than the deep soil is that the heat transferred from the top to the bottom of the active layer at this time results in downward movement of the melting front and downward migration of the melted water under the action of gravity. (2) May–June: the water content of shallow soil (0–7 cm, 7–28 cm) gradually decreased, the water content of the third layer of soil was basically unchanged, and the water content of the fourth layer of deep soil continued to increase. On the one hand, the further increase in temperature constantly melted the underground ice. On the other hand, the absorption water effects from the ground of vegetation consumed a large amount of melted water. However, since the vegetation cover is still low and the vegetation is only in the early stage of growth, the melted water in only shallow soil in this period decreased due to the absorption of vegetation, and the deep soil water after melting still continued to increase. (3) June–July: With the increase in the vegetation coverage area, the further growth of vegetation, and the enhancement in soil water evaporation from the rise in temperature, the water content of each soil layer gradually decreased, especially that of the first three layers decreased more rapidly.

The changes in the water content of each soil layer from April 2020 to July 2020 also reflect that the subsurface ice in the study area is melting continuously during the period before and after the collapse of the oil tank. This persistent subsurface ice melting process brings about the seasonal sinking, which is consistent with the characteristics of seasonal melting and sinking changes in summer as shown in Figure 6b.

4.5. Effect of Terrain Slope on the Rate of Surface Deformation

In this paper, we use ALOS DSM with 30 m spatial resolution as the surface elevation data to calculate the terrain slope. As shown in Figure 9, we statistically calculated the scattering diagram between the topographic slope and surface deformation rate. Figure 9a,b appear that the average deformation rates in the western region and the central tank collapse area are approximate −60 mm/year and 0 mm/year, respectively. When the slope is less than 15°, the surface deformation rates of the two regions fluctuate around the average values. However, when the slope is greater than 15°, the subsidence area accounts for significantly more than the lifting area. In addition, the subsidence amplitudes

in the large slope areas also increase compared with the gentle slope area (<15°). These results reflect that surface subsidence hazards are more likely to occur in areas with large topographic slopes. Moreover, Figure 10 qualitatively compared the relationship between slope and deformation rate, also supporting that the surface deformation rate is greater (>15°) in areas with sloping terrain than in the surrounding flat areas. This may be because the land surface is repeatedly frozen and thawed over the seasonal change. The melted snow and ice are more likely to drive the soil to slide in the sloping areas (>15°), thus finally causing the loosening and subsidence of the permafrost surface.
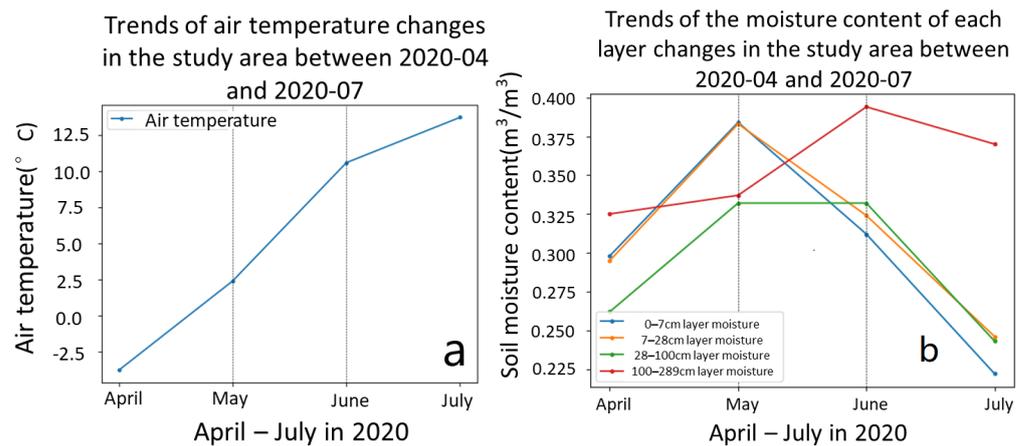
Figure 8. Trends of the average monthly air temperature and soil moisture content for the period April 2020–July 2020: (**a**) the average monthly air temperature; (**b**) the soil moisture content.
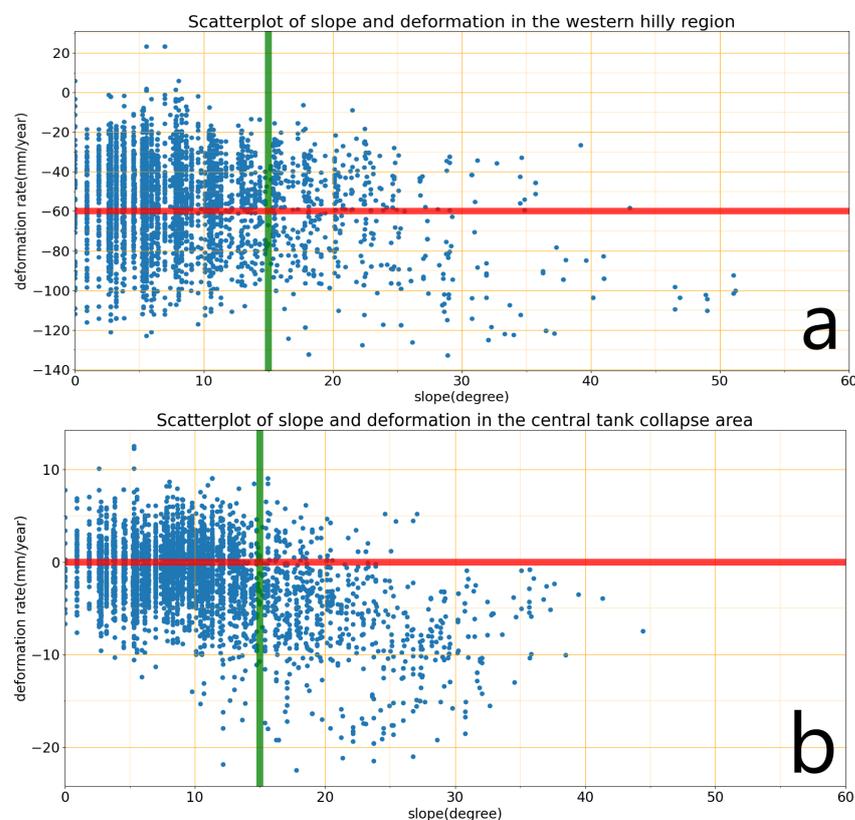
Figure 9. The scatterplot results between surface deformation rate and terrain slope from randomly selecting 5000 points in the following areas: (**a**) the western hill area; and (**b**) the central tank collapse area.
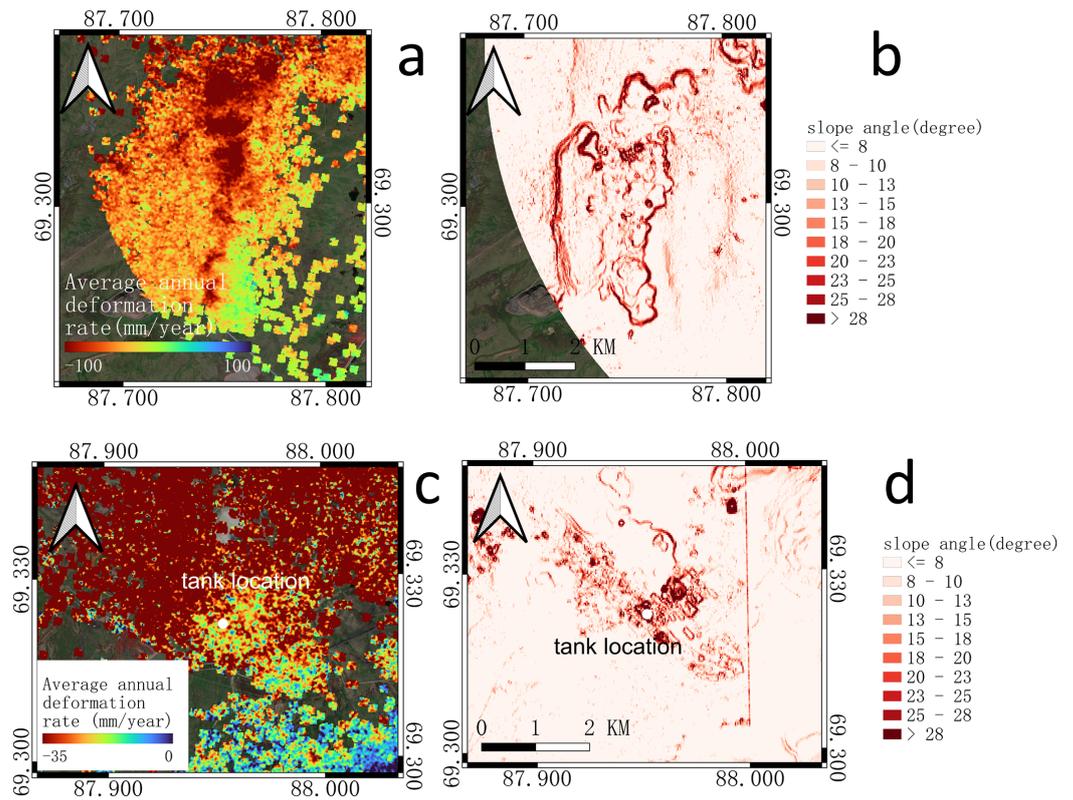
Figure 10. Comparison analysis of surface deformation rate and topographic slope in the study area based on GEE and QGIS platform: (**a**) the distribution of topographic slope in the western hilly region; (**b**) the rate of surface deformation in the western hills; (**c**) the results of topographic slope distribution in the central tank collapse area; (**d**) the distribution of surface deformation rate in the central tank collapse area.

5. Discussion

5.1. Permafrost Surface Deformation Mechanisms

Based on the above experimental results, we analyze and conclude why the oil tank collapsed. Figure 11 unveils the reasons.
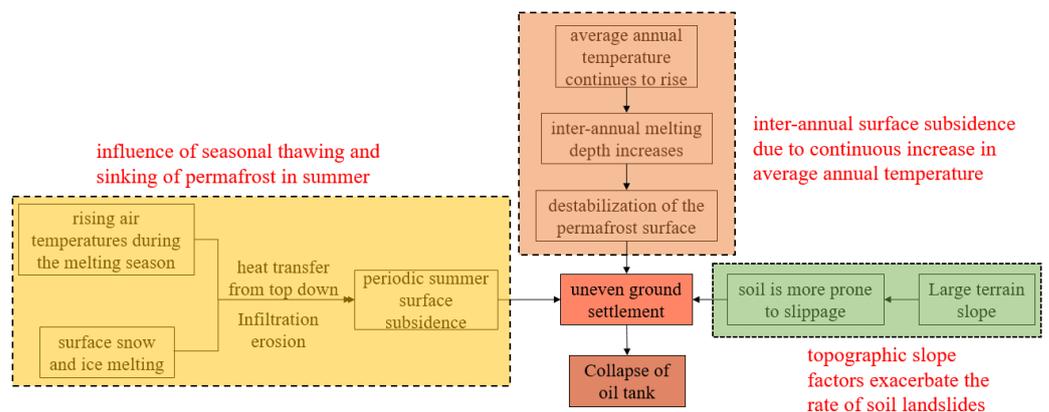
Figure 11. The analysis schematic diagram of oil tank collapse causes.

(1) The influence of a sustained increase in the annual average temperature on interannual surface subsidence.

The continuous increase in the annual mean temperature (at a rate of 2 °C/year during 2018–2020) (Figure 7b) of the area near the tank collapse site deepens the interannual melting depths (Figure 7a) and shifts the permafrost table downwards. Moreover, the continuous accumulation of the above mentioned factors resulted in surface subsidence

(Figure 6c) during 2018–2020, finally destroying the original surface stability in the tank collapse area.

(2) The influence of melting permafrost ice on seasonal subsidence in summer.

The seasonal deformation characteristics of permafrost are summer subsidence and winter uplift (Figure 6c). It is noteworthy that the moment of oil tank collapse is exactly in the permafrost summer thawing and sinking stage, where the air temperature gradually increases (Figure 8a). During this period, the heat constantly transfers from the top to the bottom of the active layer, which is only in the heat-absorption state, moving down the thawing front and melting the underground ice. Additionally, down filtration erosion of surface snowmelt also accelerates the above process. As this course ceaselessly develops during summer, seasonal subsidence trends persistently accumulate, aggravating permafrost land surface instability.

(3) Topographic slope factors also exacerbate the oil tank landslide rate.

The land surface in the tank collapse area is repeatedly frozen and thawed along with the seasonal change. More importantly, the melted snow and ice in relatively more sloped areas more easily drive soil body sliding, finally increasingly generating the ground surface to sink (Figure 10). Therefore, the topographic slope is also a non-negligible important factor for the tank collapse.

In summary, the joint effects of the abovementioned three factors eventually collapsed the oil tank in May 2020 and lowered the land surface by approximately 70–80 mm relative to that in August 2018. Furthermore, based on the analysis, we can deduce that surface deformation in the permafrost region tends to be triggered by the combined effect of increasing annual average air temperature, seasonal thawing and sinking, and topographic slope factors.

5.2. Permafrost Early Deformation Signals

In the context of climate warming, a series of permafrost degradation problems, such as an increase in active layer thickness and a reduction in permafrost area, may become serious cumulatively. The final consequence is that the resulting surface deformation poses a serious threat to the stability of buildings on permafrost. Therefore, it is of great significance to delineate severe deformation regions and prevent possible disasters such as infrastructure collapse, foundation deformation, and landslides contributed by permafrost degradation beforehand. Monitoring permafrost surface deformation can take precautions in advance to prevent surface deformation hazards from permafrost degradation. However, the characteristics of surface deformation monitoring techniques requiring predetermined monitoring areas and monitoring time constrain their use in permafrost deformation monitoring. This paper selected and analyzed the oil tank collapse accident in the Norilsk region. We find that when the annual average temperature continues to rise at a rate of 2 °C/year for 2∼3 consecutive years, permafrost regions with large topographic slopes (>15°) are more prone to surface deformation disasters during the summer thaw. Therefore, we suggest taking "the annual mean temperature continues to increase at a rate of 2 °C/year for 2∼3 consecutive years" as an early surface deformation signal of permafrost degradation disasters. Furthermore, when the signal is detected, it is necessary to use surface deformation monitoring techniques for relatively more sloped areas (>15°) during permafrost thaw to monitor the deformation rate and delineate severe deformation regions. These conclusions can help predetermine the monitoring areas and monitoring time in advance and improve deformation monitoring techniques' effectiveness.

5.3. Comparison with Previous Studies

We first compare our experimental results with those of others. As mentioned in Section 4.1, the deformation rate in the study area of this paper is −30 mm/year on average and −280 mm/year on maximum. Reference [20] showed that the subsidence rate in permafrost with built-up expressways could reach −0.318 m/year in the first 3 years. We dissect the great discrepancy in results comes mainly from the fact that the study object in

reference [20] was conducted on a newly established highway. Heavy vehicles and goods would increase the effective stress on the ground surface and reduce the soil porosity, resulting in non-plastic subsidence deformation and eventually large subsidence. Therefore, its pavement subsidence rate is larger. References [2,55] displayed the average permafrost surface deformation rates were −15 mm/year and −5∼−20 mm/year, respectively, which are close to the results of our paper. These results from references [2,55] support the accuracy of the deformation results in our paper. Moreover, it is also further reasoned that the permafrost with new-established highways has greater deformation rates than other permafrost zones. This paper also uses the Stefan model to calculate melting depth. The values of melting depth calculated in references [56,57] were in the range of 1–5 m and 1–2.5 m, respectively. As shown in Figure 7a of Section 4.3, the melting depth calculated in our paper (1.6–2.4 m) is exactly in these ranges. This comparison can reflect the accuracy of the melting depth results of this paper from the side.

Additionally, this paper also makes comparisons between our conclusions and those of others and analyzes the reasons for the differences. References [18,19] indicated deepening inter-annual thaw depth and seasonal deformation could destabilize the permafrost surface. Reference [20] mentioned topographic factors also would influence permafrost deformation. The above mentioned references support conclusions in Section 5.1. Unlike this paper, which identifies severe deformation areas from the perspective of annual average temperature change (in Section 5.2). Reference [58] concluded that surface settlement would be greater in areas where the mean annual ground temperatures (MAGT) were greater than −1.5 °C from the perspective of the MAGT spatial distribution. Although the perspectives are different, it is clear that temperature factors do result in a dramatic deformation of the ground surface. Furthermore, high or increasing temperatures are important factors affecting permafrost deformation and stability distribution. Reference [55] emphasized the areas where the slope angle exceeds (>10°) are more prone to deformation accidents, while this value is (>15°) in this paper. There is a slight difference in the values between the two. The source of the difference may be partly from the different study areas and partly from the subjectivity of the researchers.

Finally, we also discuss the differences in focus from previous studies. Generally, previous studies on permafrost deformation mechanisms tend to have two characteristics: (1) the research objects mainly focus on the embankments of expressways and railways on permafrost; (2) the research results on deformation mechanisms are not closely integrated with existing deformation monitoring techniques. For instance, the embankments of expressways and railways on permafrost were studied in references [58–61] to illustrate the permafrost deformation mechanisms, nevertheless, none of these papers further integrated the results with existing deformation monitoring techniques. Although the occurrence mechanisms of permafrost deformation have been clarified, the insufficient application of the influencing factors of permafrost deformation to the existing deformation monitoring techniques makes the current monitoring of permafrost surface deformation hazards still mainly after-the-fact monitoring and difficult to prevent in advance. This paper specifically addresses the problem that the existing deformation monitoring technology requires monitoring areas and monitoring time in advance. Based on the study of the permafrost deformation mechanisms, we propose the early surface deformation signals to predetermine the monitoring area and monitoring time from each deformation influencing factor and realize the combination of the permafrost deformation mechanisms and the existing deformation monitoring techniques.

5.4. Limitation and Future Reasearch

Although some valuable contributions have been made in this paper, this work has limitations. As noted, we only focused on an oil tank collapse accident, and this is to say the study case and study area are both singular, which restricts the applicability of the proposed permafrost surface deformation hazard monitoring and early warning method on a global scale. Moreover, from the lack of field observations, the experimental results in

this paper are only roughly compared with previous studies to illustrate the accuracy of the results. The crudeness of this experimental verification may lead to unreliable conclusions. However, there are few sharable cases of surface deformation hazards from permafrost degradation, such as oil tank collapse, globally; thus, collecting and building a global case analysis library of surface deformation hazards in various types of permafrost will help to comprehend the permafrost surface deformation mechanism and enrich and improve surface deformation hazard monitoring techniques.

6. Conclusions

Examining and analyzing oil tank collapse accidents, this paper analyzes early surface deformation signals and discusses how to predetermine the location and time of possibly occurring severe surface deformation before employing surface deformation monitoring techniques. In this paper, we first apply the SBAS-InSAR technique to obtain the deformation rate of the study area. Then, we utilize a sine model to decompose interannual deformation and seasonal deformation and compare the relationship between topographic slope and surface deformation rate. Finally, we find that the reasons for deformation disasters such as tank collapse triggered by permafrost degradation mainly include three aspects: increasing the annual temperature deepens the interannual melting depth, the summer thaw period causes periodic settlement, and the topographic slope exacerbates landslides. More specifically, this paper reveals that when the annual mean temperature of the permafrost region continues to increase at a rate of 2 °C/year for 2~3 consecutive years, areas with relatively large topographic slopes (>15°) are more prone to surface deformation disasters during the summer thaw period. Therefore, this paper suggests that permafrost areas with large topographic slopes (>15°) should be taken as the key surveillance areas, and that the appropriate monitoring time for employing surface deformation monitoring techniques should be the summer thawing period after a continuous increase in annual average temperature at a rate of 2 °C/year for 2~3 years.

References

1. Liu, S.; Zhao, L.; Wang, L.; Zhou, H.; Zou, D.; Sun, Z.; Xie, C.; Qiao, Y. Intra-Annual Ground Surface Deformation Detected by Site Observation, Simulation and InSAR Monitoring in Permafrost Site of Xidatan, Qinghai-Tibet Plateau. *Geophys. Res. Lett.* **2022**, *49*, e2021GL095029. [CrossRef]
2. Wang, L.; Zhao, L.; Zhou, H.; Liu, S.; Du, E.; Zou, D.; Liu, G.; Wang, C.; Li, Y. Permafrost Ground Ice Melting and Deformation Time Series Revealed by Sentinel-1 InSAR in the Tanggula Mountain Region on the Tibetan Plateau. *Remote Sens.* **2022**, *14*, 811. [CrossRef]
3. Meng, Q.; Intrieri, E.; Raspini, F.; Peng, Y.; Liu, H.; Casagli, N. Satellite-based interferometric monitoring of deformation characteristics and their relationship with internal hydrothermal structures of an earthflow in Zhimei, Yushu, Qinghai-Tibet Plateau. *Remote Sens. Environ.* **2022**, *273*, 112987. [CrossRef]
4. IPCC Climate Change. The physical science basis. In *Contribution of Working Group I to the Fifth Assessment Report of the Intergovernmental Panel on Climate Change*; IPCC: Geneva, Switzerland, 2013; Volume 1535, p. 2013.
5. Schuur, E.A.; McGuire, A.D.; Schädel, C.; Grosse, G.; Harden, J.W.; Hayes, D.J.; Hugelius, G.; Koven, C.D.; Kuhry, P.; Lawrence, D.M.; et al. Climate change and the permafrost carbon feedback. *Nature* **2015**, *520*, 171–179. [CrossRef] [PubMed]
6. Walter Anthony, K.; Schneider von Deimling, T.; Nitze, I.; Frolking, S.; Emond, A.; Daanen, R.; Anthony, P.; Lindgren, P.; Jones, B.; Grosse, G. 21st-century modeled permafrost carbon emissions accelerated by abrupt thaw beneath lakes. *Nat. Commun.* **2018**, *9*, 3262. [CrossRef] [PubMed]
7. Chen, H.; Zhu, Q.; Peng, C.; Wu, N.; Wang, Y.; Fang, X.; Gao, Y.; Zhu, D.; Yang, G.; Tian, J.; et al. The impacts of climate change and human activities on biogeochemical cycles on the Q inghai-T ibetan P lateau. *Glob. Chang. Biol.* **2013**, *19*, 2940–2955. [CrossRef]
8. Woodcroft, B.J.; Singleton, C.M.; Boyd, J.A.; Evans, P.N.; Emerson, J.B.; Zayed, A.A.; Hoelzle, R.D.; Lamberton, T.O.; McCalley, C.K.; Hodgkins, S.B.; et al. Genome-centric view of carbon processing in thawing permafrost. *Nature* **2018**, *560*, 49–54. [CrossRef] [PubMed]
9. Qhma, B.; Ji, C.; Jcw, C.; Xin, H.; Jyz, A.; Shz, C.; C, H.; Jwga, B. Strengthening effect of crushed rock revetment and thermosyphons in a traditional embankment in permafrost regions under warming climate. *Adv. Clim. Chang. Res.* **2021**, *12*, 66–75.
10. Wang, S.; Niu, F.; Chen, J.; Dong, Y. Permafrost research in China related to express highway construction. *Permafr. Periglac. Process.* **2020**, *31*, 406–416. [CrossRef]
11. Zhong, W.; Zhang, T.; Chen, J.; Shang, J.; Wang, S.; Mu, C.; Fan, C. Seasonal deformation monitoring over thermokarst landforms using terrestrial laser scanning in Northeastern Qinghai-Tibetan Plateau. *Int. J. Appl. Earth Obs. Geoinf.* **2021**, *103*, 102501. [CrossRef]
12. Li, R.; Li, Z.; Han, J.; Lu, P.; Qiao, G.; Meng, X.; Hao, T.; Zhou, F. Monitoring surface deformation of permafrost in Wudaoliang Region, Qinghai–Tibet Plateau with ENVISAT ASAR data. *Int. J. Appl. Earth Obs. Geoinf.* **2021**, *104*, 102527. [CrossRef]
13. Howard, H.R.; Manandhar, S.; Wang, Q.; Mcmillan, J.M.; Qie, G.; Liu, X.; Thapa, K.; Xu, X.; Wang, G. Spatially characterizing land surface deformation and permafrost active layer thickness for Donnelly installation of Alaska using DInSAR and MODIS data. *Cold Reg. Sci. Technol.* **2022**, *196*, 103510. [CrossRef]
14. Luo, L.; Zhuang, Y.; Zhang, M.; Zhang, Z.; Ma, W.; Zhao, W.; Zhao, L.; Wang, L.; Shi, Y.; Zhang, Z.; et al. An integrated observation dataset of the hydrological and thermal deformation in permafrost slopes and engineering infrastructure in the Qinghai–Tibet Engineering Corridor. *Earth Syst. Sci. Data* **2021**, *13*, 4035–4052. [CrossRef]
15. Chai, M.; Li, G.; Ma, W.; Cao, Y.; Wu, G.; Mu, Y.; Chen, D.; Zhang, J.; Zhou, Z.; Zhou, Y.; et al. Assessment of freeze–thaw hazards and water features along the China–Russia Crude Oil Pipeline in permafrost regions. *Remote Sens.* **2020**, *12*, 3576. [CrossRef]
16. Shi, X.; Jiang, L.; Jiang, H.; Wang, X.; Xu, J. Geohazards Analysis of the Litang–Batang Section of Sichuan–Tibet Railway Using SAR Interferometry. *IEEE J. Sel. Top. Appl. Earth Obs. Remote Sens.* **2021**, *14*, 11998–12006. [CrossRef]
17. Shan, W.; Hu, Z.; Jiang, H.; Guo, Y.; Wang, C. Environmental and Engineering Geology of the Bei'an to Heihe Expressway in China with a Focus on Climate Change. In *Engineering Geology for Society and Territory*; Springer: Cham, Switzerland, 2015; Volume 1, pp. 271–277.
18. Qi, J.; Sheng, Y.; Zhang, J.; Wen, Z. Settlement of embankments in permafrost regions in the Qinghai-Tibet Plateau. *Nor. Geogr. Tidsskr.-Nor. J. Geogr.* **2007**, *61*, 49–55.
19. Yuan, C.; Yu, Q.; You, Y.; Guo, L. Deformation mechanism of an expressway embankment in warm and high ice content permafrost regions. *Appl. Therm. Eng.* **2017**, *121*, 1032–1039. [CrossRef]
20. Luo, X.; Yu, Q.; Ma, Q.; Guo, L. Study on the heat and deformation characteristics of an expressway embankment with shady and sunny slopes in warm and ice-rich permafrost regions. *Transp. Geotech.* **2020**, *24*, 100390. [CrossRef]
21. Wang, S.; Chen, Z.; Qin, W.; Liu, Y.; Liu, F.; Jin, G. Using DInSAR to Monitor Frost Heaving and Thaw Settlement Deformation of Highway Subgrade in Seasonal Frozen Soil Zone. *J. Wuhan Univ. Technol. (Transp. Sci. Eng.)* **2018**, *42*, 58–62.
22. Wang, H.; Qi, Y.; Zhang, J.; Zhang, J.; Yang, R.; Guo, J.; Luo, D.; Wu, J.; Zhou, S. Influence of Open-Pit Coal Mining on Ground Surface Deformation of Permafrost in the Muli Region in the Qinghai-Tibet Plateau, China. *Remote Sens.* **2022**, *14*, 2352. [CrossRef]
23. Luo, L.; Ma, W.; Zhang, Z.; Zhuang, Y.; Zhang, Y.; Yang, J.; Cao, X.; Liang, S.; Mu, Y. Freeze/thaw-induced deformation monitoring and assessment of the slope in permafrost based on terrestrial laser scanner and GNSS. *Remote Sens.* **2017**, *9*, 198. [CrossRef]
24. Kenyi, L.W.; Kaufmann, V. Estimation of rock glacier surface deformation using SAR interferometry data. *IEEE Trans. Geosci. Remote Sens.* **2003**, *41*, 1512–1515. [CrossRef]

25. Echelard, T.; Krysiecki, J.M.; Gay, M.; Schoeneich, P. Rockglacier movements detection by Differential Interferometric Synthetic Aperture Radar D-InSAR in French Alps using ERS (European Remote Sensing) archive data. *Geomorphol.-Relief Process. Environ.* **2013**, *3*, 231–242. [CrossRef]

26. Kunz, J.; Ullmann, T.; Kneisel, C. Internal structure and recent dynamics of a moraine complex in an alpine glacier forefield revealed by geophysical surveying and Sentinel-1 InSAR time series. *Geomorphology* **2022**, *398*, 108052. [CrossRef]

27. Zou, L.; Wang, C.; Tang, Y.; Zhang, B.; Zhang, H.; Dong, L. Interferometric SAR Observation of Permafrost Status in the Northern Qinghai-Tibet Plateau by ALOS, ALOS-2 and Sentinel-1 between 2007 and 2021. *Remote Sens.* **2022**, *14*, 1870. [CrossRef]

28. LI, S.S.; LI, Z.W.; Hu, J.; Sun, Q.; YU, X.Y. Investigation of the seasonal oscillation of the permafrost over Qinghai-Tibet Plateau with SBAS-InSAR algorithm. *Chin. J. Geophys.* **2013**, *56*, 1476–1486.

29. Chen, J.; Wu, T.; Zou, D.; Liu, L.; Wu, X.; Gong, W.; Zhu, X.; Li, R.; Hao, J.; Hu, G.; et al. Magnitudes and patterns of large-scale permafrost ground deformation revealed by Sentinel-1 InSAR on the central Qinghai-Tibet Plateau. *Remote Sens. Environ.* **2022**, *268*, 112778. [CrossRef]

30. Weise, E.; Karina Zaiets, K.G. Russia Declares State of Emergency over Arctic Circle Oil Spill Caused by Melting Permafrost. (USA TODAY). 2020. Available online: https://www.usatoday.com/in-depth/graphics/2020/06/05/oil-spill-red-river-permafrost-tied-russian-arctic-circle-emergency-diesel/3143679001/ (accessed on 6 June 2020).

31. Seddon, M. Siberia Fuel Spill Threatens Moscow's Arctic Ambitions. (Financial Times). 2020. Available online: https://www.ft.com/content/fa9c20a0-2dad-4992-9686-0ec98b44faa8 (accessed on 4 June 2020).

32. Kozhevnikov, D. Diesel Fuel Spill in Norilsk in Russia's Arctic Contained. (TASS, Moscow, Russia). 2020. Available online: https://tass.com/emergencies/1164423#:~:text=Cleanup%20workers%20have%20contained%20the,collected%2C%22%20the%20ministry%20said (accessed on 5 June 2020).

33. Rajendran, S.; Sadooni, F.N.; Al-Kuwari, H.A.S.; Oleg, A.; Govil, H.; Nasir, S.; Vethamony, P. Monitoring oil spill in Norilsk, Russia using satellite data. *Sci. Rep.* **2021**, *11*, 3817. [CrossRef]

34. Iljin, K. Remediation after Oil Spill in Norilsk Will Cost $2 Billion. (BBC News Russia). 2020. Available online: https://www.bbc.com/russian/features-53282724 (accessed on 18 October 2020).

35. Shur, Y.L.; Jorgenson, M.T. Patterns of permafrost formation and degradation in relation to climate and ecosystems. *Permafr. Periglac. Process.* **2007**, *18*, 7–19. [CrossRef]

36. Ran, Y.; Jorgenson, M.T.; Li, X.; Jin, H.; Wu, T.; Li, R.; Cheng, G. *A Biophysical Permafrost Zonation Map in the Northern Hemisphere (2000–2016)*; National Tibetan Plateau Data Center: Beijing, China, 2021. [CrossRef]

37. Ran, Y.; Jorgenson, M.T.; Li, X.; Jin, H.; Wu, T.; Li, R.; Cheng, G. Biophysical permafrost map indicates ecosystem processes dominate permafrost stability in the Northern Hemisphere. *Environ. Res. Lett.* **2021**, *16*, 095010. [CrossRef]

38. Ran, Y.; Li, X.; Cheng, G.; Che, J.; Aalto, J.; Karjalainen, O.; Hjort, J.; Luoto, M.; Jin, H.; Obu, J.; et al. New high-resolution estimates of the permafrost thermal state and hydrothermal conditions over the Northern Hemisphere. *Earth Syst. Sci. Data* **2022**, *14*, 865–884. [CrossRef]

39. Dai, Y.; Wei, N.; Yuan, H.; Zhang, S.; Shangguan, W.; Liu, S.; Lu, X.; Xin, Y. Evaluation of soil thermal conductivity schemes for use in land surface modeling. *J. Adv. Model. Earth Syst.* **2019**, *11*, 3454–3473. [CrossRef]

40. Dai, Y.; Xin, Q.; Wei, N.; Zhang, Y.; Shangguan, W.; Yuan, H.; Zhang, S.; Liu, S.; Lu, X. A Global High-Resolution Data Set of Soil Hydraulic and Thermal Properties for Land Surface Modeling. *J. Adv. Model. Earth Syst.* **2019**, *11*, 2996–3023. [CrossRef]

41. Ferretti, A.; Prati, C. Nonlinear subsidence rate estimation using permanent scatterers in differential SAR interferometry. *IEEE Trans. Geosci. Remote Sens.* **2000**, *38*, 2202–2212. [CrossRef]

42. Berardino, P.; Fornaro, G.; Lanari, R.; Sansosti, E. A new algorithm for surface deformation monitoring based on small baseline differential SAR interferograms. *IEEE Trans. Geosci. Remote Sens.* **2002**, *40*, 2375–2383. [CrossRef]

43. Goldstein, R.M.; Zebker, H.A.; Werner, C.L. Satellite radar interferometry: Two-dimensional phase unwrapping. *Radio Sci.* **1988**, *23*, 713–720. [CrossRef]

44. Costantini, M. A novel phase unwrapping method based on network programming. *IEEE Trans. Geosci. Remote Sens.* **1998**, *36*, 813–821. [CrossRef]

45. Daout, S.; Doin, M.P.; Peltzer, G.; Socquet, A.; Lasserre, C. Large-scale InSAR monitoring of permafrost freeze-thaw cycles on the Tibetan Plateau. *Geophys. Res. Lett.* **2017**, *44*, 901–909. [CrossRef]

46. Li, Z.; Zhao, R.; Hu, J.; Wen, L.; Feng, G.; Zhang, Z.; Wang, Q. InSAR analysis of surface deformation over permafrost to estimate active layer thickness based on one-dimensional heat transfer model of soils. *Sci. Rep.* **2015**, *5*, 15542. [CrossRef]

47. Johansen, O. Thermal Conductivity of Soils. Ph.D. Thesis, Trondheim University, Trondheim, Norway, 1977.

48. Kersten, M.S. *Laboratory Research for the Determination of Thermal Properties of Soils*; Arctic Construction and Frost Effects Laboratory (US): Boston, MA, USA, 1949.

49. Balland, P.V. Modeling soil thermal conductivities over a wide range of conditions. *J. Environ. Eng. Sci.* **2005**, *4*, 549–558. [CrossRef]

50. Stefan, J. Über die Theorie der Eisbildung, insbesondere über die Eisbildung im Polarmeere. *Ann. Phys.* **1891**, *278*, 269–286. [CrossRef]

51. Klene, A.E.; Nelson, F.E.; Shiklomanov, N.I.; Hinkel, K.M. The n-factor in natural landscapes: Variability of air and soil-surface temperatures, Kuparuk River Basin, Alaska, USA. *Arctic Antarct. Alp. Res.* **2001**, *33*, 140–148. [CrossRef]

52. Lunardini, V.J. *Heat Transfer in Cold Climates*; Van Nostrand Reinhold Company: New York, NY, USA, 1981.

53. Kurylyk, B.L.; McKenzie, J.M.; MacQuarrie, K.T.; Voss, C.I. Analytical solutions for benchmarking cold regions subsurface water flow and energy transport models: One-dimensional soil thaw with conduction and advection. *Adv. Water Resour.* **2014**, *70*, 172–184. [CrossRef]

54. Jumikis, A.R. Thermal geotechnics. *Soil Sci.* **1978**, *125*, 393. [CrossRef]

55. Rouyet, L.; Karjalainen, O.; Niittynen, P.; Aalto, J.; Luoto, M.; Lauknes, T.R.; Larsen, Y.; Hjort, J. Environmental Controls of InSAR-Based Periglacial Ground Dynamics in a Sub-Arctic Landscape. *J. Geophys. Res. Earth Surf.* **2021**, *126*, e2021JF006175. [CrossRef]

56. Qi, Y.; Li, S.; Ran, Y.; Wang, H.; Wu, J.; Lian, X.; Luo, D. Mapping frozen ground in the Qilian Mountains in 2004–2019 using Google earth engine cloud computing. *Remote Sens.* **2021**, *13*, 149. [CrossRef]

57. Cao, H.; Gao, B.; Gong, T.; Wang, B. Analyzing changes in frozen soil in the source region of the yellow river using the modis land surface temperature products. *Remote Sens.* **2021**, *13*, 180. [CrossRef]

58. Ma, W.; Mu, Y.; Wu, Q.; Sun, Z.; Liu, Y. Characteristics and mechanisms of embankment deformation along the Qinghai–Tibet Railway in permafrost regions. *Cold Reg. Sci. Technol.* **2011**, *67*, 178–186. [CrossRef]

59. Ming, F.; Yu, Q.h.; Li, D.Q. Investigation of embankment deformation mechanisms in permafrost regions. *Transp. Geotech.* **2018**, *16*, 21–28. [CrossRef]

60. Yu, F.; Qi, J.; Lai, Y.; Sivasithamparam, N.; Yao, X.; Zhang, M.; Liu, Y.; Wu, G. Typical embankment settlement/heave patterns of the Qinghai–Tibet highway in permafrost regions: Formation and evolution. *Eng. Geol.* **2016**, *214*, 147–156. [CrossRef]

61. Tai, B.; Wu, Q.; Zhang, Z.; Xu, X. Cooling performance and deformation behavior of crushed-rock embankments on the Qinghai-Tibet Railway in permafrost regions. *Eng. Geol.* **2020**, *265*, 105453. [CrossRef]